Published in "Nature 466: 213-216, 2010"
which should be cited to refer to this work.

The size of the proton

Randolf Pohl[1], Aldo Antognini[1], François Nez[2], Fernando D. Amaro[3], François Biraben[2], João M. R. Cardoso[3], Daniel S. Covita[3,4], Andreas Dax[5], Satish Dhawan[5], Luis M. P. Fernandes[3], Adolf Giesen[6]†, Thomas Graf[6], Theodor W. Hänsch[1], Paul Indelicato[2], Lucile Julien[2], Cheng-Yang Kao[7], Paul Knowles[8], Eric-Olivier Le Bigot[2], Yi-Wei Liu[7], José A. M. Lopes[3], Livia Ludhova[8], Cristina M. B. Monteiro[3], Françoise Mulhauser[8]†, Tobias Nebel[1], Paul Rabinowitz[9], Joaquim M. F. dos Santos[3], Lukas A. Schaller[8], Karsten Schuhmann[10], Catherine Schwob[2], David Taqqu[11], João F. C. A. Veloso[4] & Franz Kottmann[12]

The proton is the primary building block of the visible Universe, but many of its properties—such as its charge radius and its anomalous magnetic moment—are not well understood. The root-mean-square charge radius, r_p, has been determined with an accuracy of 2 per cent (at best) by electron–proton scattering experiments[1,2]. The present most accurate value of r_p (with an uncertainty of 1 per cent) is given by the CODATA compilation of physical constants[3]. This value is based mainly on precision spectroscopy of atomic hydrogen[4–7] and calculations of bound-state quantum electrodynamics (QED; refs 8, 9). The accuracy of r_p as deduced from electron–proton scattering limits the testing of bound-state QED in atomic hydrogen as well as the determination of the Rydberg constant (currently the most accurately measured fundamental physical constant[3]). An attractive means to improve the accuracy in the measurement of r_p is provided by muonic hydrogen (a proton orbited by a negative muon); its much smaller Bohr radius compared to ordinary atomic hydrogen causes enhancement of effects related to the finite size of the proton. In particular, the Lamb shift[10] (the energy difference between the $2S_{1/2}$ and $2P_{1/2}$ states) is affected by as much as 2 per cent. Here we use pulsed laser spectroscopy to measure a muonic Lamb shift of 49,881.88(76) GHz. On the basis of present calculations[11–15] of fine and hyperfine splittings and QED terms, we find $r_p = 0.84184(67)$ fm, which differs by 5.0 standard deviations from the CODATA value[3] of 0.8768(69) fm. Our result implies that either the Rydberg constant has to be shifted by $-110\,\mathrm{kHz}/c$ (4.9 standard deviations), or the calculations of the QED effects in atomic hydrogen or muonic hydrogen atoms are insufficient.

Bound-state QED was initiated in 1947 when a subtle difference between the binding energies of the $2S_{1/2}$ and $2P_{1/2}$ states of H atoms was established, denoted as the Lamb shift[10]. It is dominated by purely radiative effects[8], such as 'self energy' and 'vacuum polarization'. More recently, precision optical spectroscopy of H atoms[4–7] and the corresponding calculations[8,9] have improved tremendously and reached a point where the proton size (expressed by its root-mean-square charge radius, $r_p = \sqrt{\langle r_p^2 \rangle}$) is the limiting factor when comparing experiment with theory[16].

The CODATA value[3] of $r_p = 0.8768(69)$ fm is extracted mainly from H atom spectroscopy and thus relies on bound-state QED (here and elsewhere numbers in parenthesis indicate the 1 s.d. uncertainty of the trailing digits of the given number). An H-independent but less precise value of $r_p = 0.897(18)$ fm was obtained in a recent reanalysis of electron-scattering experiments[1,2].

A much better determination of the proton radius is possible by measuring the Lamb shift in muonic hydrogen (μp, an atom formed by a proton, p, and a negative muon, μ^-). The muon is about 200 times heavier than the electron. The atomic Bohr radius is correspondingly about 200 times smaller in μp than in H. Effects of the finite size of the proton on the muonic S states are thus enhanced. S states are shifted because the muon's wavefunction at the location of the proton is non-zero. In contrast, P states are not significantly shifted. The total predicted $2S_{1/2}^{F=1} - 2P_{3/2}^{F=2}$ energy difference, $\Delta\tilde{E}$, in muonic hydrogen is the sum of radiative, recoil, and proton structure contributions, and the fine and hyperfine splittings for our particular transition, and it is given[8,11–15] by

$$\Delta\tilde{E} = 209.9779(49) - 5.2262\ r_p^2 + 0.0347\ r_p^3\ \mathrm{meV} \qquad (1)$$

where $r_p = \sqrt{\langle r_p^2 \rangle}$ is given in fm. A detailed derivation of equation (1) is given in Supplementary Information.

The first term in equation (1) is dominated by vacuum polarization, which causes the 2S states to be more tightly bound than the 2P states (Fig. 1). The μp fine and hyperfine splittings (due to spin–orbit and spin–spin interactions) are an order of magnitude smaller than the Lamb shift (Fig. 1c). The uncertainty of 0.0049 meV in $\Delta\tilde{E}$ is dominated by the proton polarizability term[13] of 0.015(4) meV. The second and third terms in equation (1) are the finite size contributions. They amount to 1.8% of $\Delta\tilde{E}$, two orders of magnitude more than for H.

For more than forty years, a measurement of the μp Lamb shift has been considered one of the fundamental experiments in atomic spectroscopy, but only recent progress in muon beams and laser technology made such an experiment feasible. We report the first successful measurement of the μp Lamb shift. The energy difference between the $2S_{1/2}^{F=1}$ and $2P_{3/2}^{F=2}$ states of μp atoms has been determined by means of pulsed laser spectroscopy at wavelengths around 6.01 μm. This transition was chosen because it gives the largest signal of all six allowed optical 2S–2P transitions. All transitions are spectrally well separated.

The experiment was performed at the πE5 beam-line of the proton accelerator at the Paul Scherrer Institute (PSI) in Switzerland. We

[1]Max-Planck-Institut für Quantenoptik, 85748 Garching, Germany. [2]Laboratoire Kastler Brossel, École Normale Supérieure, CNRS, and Université P. et M. Curie-Paris 6, 75252 Paris, Cedex 05, France. [3]Departamento de Física, Universidade de Coimbra, 3004-516 Coimbra, Portugal. [4]I3N, Departamento de Física, Universidade de Aveiro, 3810-193 Aveiro, Portugal. [5]Physics Department, Yale University, New Haven, Connecticut 06520-8121, USA. [6]Institut für Strahlwerkzeuge, Universität Stuttgart, 70569 Stuttgart, Germany. [7]Physics Department, National Tsing Hua University, Hsinchu 300, Taiwan. [8]Département de Physique, Université de Fribourg, 1700 Fribourg, Switzerland. [9]Department of Chemistry, Princeton University, Princeton, New Jersey 08544-1009, USA. [10]Dausinger & Giesen GmbH, Rotebühlstr. 87, 70178 Stuttgart, Germany. [11]Paul Scherrer Institute, 5232 Villigen-PSI, Switzerland. [12]Institut für Teilchenphysik, ETH Zürich, 8093 Zürich, Switzerland. †Present addresses: Deutsches Zentrum für Luft- und Raumfahrt e.V. in der Helmholtz-Gemeinschaft, 70569 Stuttgart, Germany (A.G.); International Atomic Energy Agency, A-1400 Vienna, Austria (F.M.).

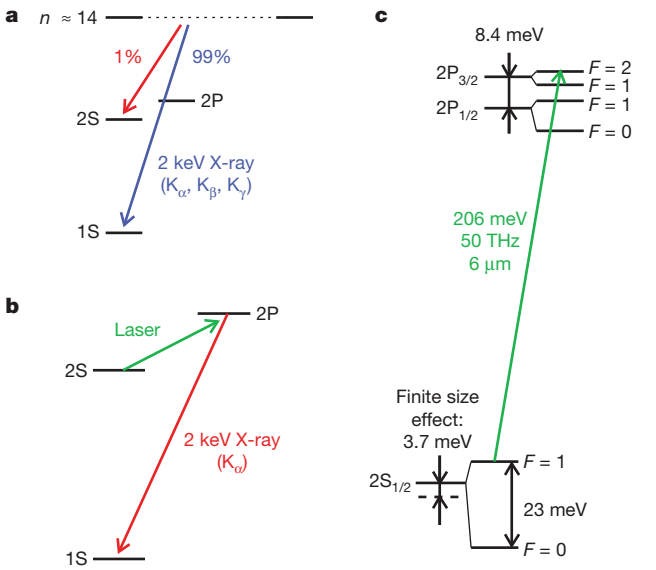

Figure 1 | Energy levels, cascade and experimental principle in muonic hydrogen. **a**, About 99% of the muons proceed directly to the 1S ground state during the muonic cascade, emitting 'prompt' K-series X-rays (blue). 1% remain in the metastable 2S state (red). **b**, The $\mu p(2S)$ atoms are illuminated by a laser pulse (green) at 'delayed' times. If the laser is on resonance, delayed K_α X-rays are observed (red). **c**, Vacuum polarization dominates the Lamb shift in μp. The proton's finite size effect on the 2S state is large. The green arrow indicates the observed laser transition at $\lambda = 6\,\mu m$.

built a new beam-line for low-energy negative muons (~5 keV kinetic energy) that yields an order of magnitude more muon stops in a small low-density gas volume than a conventional muon beam[17]. Slow μ^- enter a 5 T solenoid and are detected in two transmission muon detectors (sketched in Fig. 2 and described in Methods), generating a trigger for the pulsed laser system.

The muons are stopped in H_2 gas at 1 hPa, whereby highly excited μp atoms ($n \approx 14$) are formed[18]. Most of these de-excite quickly to the 1S ground state[19], but ~1% populate the long-lived 2S state[20] (Fig. 1a). A short laser pulse with a wavelength tunable around $\lambda \approx 6\,\mu m$ enters the mirror cavity[21] surrounding the target gas volume, about 0.9 μs after the muon stop. 2S⟶2P transitions are induced on resonance (Fig. 1b), immediately followed by 2P⟶1S de-excitation via emission of a 1.9 keV X-ray (lifetime $\tau_{2P} = 8.5$ ps). A resonance curve is obtained by measuring at different laser wavelengths the number of 1.9 keV X-rays that occur in time-coincidence with the laser pulse. The laser fluence of 6 mJ cm^{-2} results in a 2S–2P transition probability on resonance of about 30%.

The lifetime of the μp 2S state, τ_{2S}, is crucial for this experiment. In the absence of collisions, τ_{2S} would be equal to the muon lifetime of 2.2 μs. In H_2 gas, however, the 2S state is collisionally quenched, so that $\tau_{2S} \approx 1\,\mu s$ at our H_2 gas pressure of 1 hPa (ref. 20). This pressure is a trade-off between maximizing τ_{2S} and minimizing the muon stop

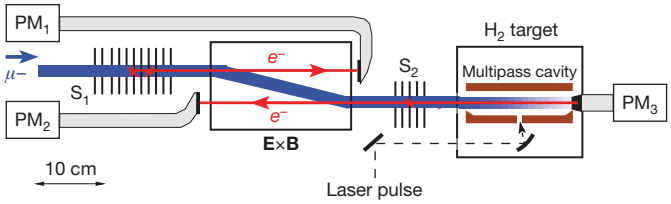

Figure 2 | Muon beam. Muons (blue) entering the final stage of the muon beam line pass two stacks of ultra-thin carbon foils (S_1, S_2). The released electrons (red) are separated from the slower muons by **E**×**B** drift in an electric field E applied perpendicularly to the $B = 5$ T magnetic field and are detected in plastic scintillators read out by photomultiplier tubes (PM_{1-3}). The muon stop volume is evenly illuminated by the laser light using a multipass cavity.

volume (length ∝ 1/pressure) and therefore the laser pulse energy required to drive the 2S–2P transition.

The design of the laser (Fig. 3 and Methods) is dictated by the need for tunable light output within τ_{2S} after a random trigger by an incoming muon with a rate of about 400 s^{-1}. The continuous wave (c.w.) light at $\lambda \approx 708$ nm of a tunable Ti:sapphire laser is pulse-amplified by frequency-doubled light from a c.w.-pumped Yb:YAG disk laser[22,23]. The c.w. Ti:sapphire laser is locked to a Fabry–Perot cavity with a free spectral range (FSR) of 1,497.332(3) MHz. The pulsed light[24,25] is shifted to $\lambda \approx 6\,\mu m$ by three sequential vibrational Stokes shifts in a Raman cell[26] filled with H_2.

Tuning the c.w. Ti:sapphire laser at $\lambda \approx 708$ nm by a frequency difference $\Delta\nu$ results in the same $\Delta\nu$ detuning of the 6 μm light after the Raman cell. During the search for the resonance, we scanned the laser in steps of typically 6 FSR ≈ 9 GHz, not to miss the 18.6-GHz-wide resonance line. The final resonance scan was performed in steps of 2 FSR. For the absolute frequency calibration, we recorded several absorption spectra of water vapour at $\lambda \approx 6\,\mu m$, thereby eliminating possible systematic shifts originating from the Ti:sapphire laser or the Raman process. By H_2O absorption, we also determined the laser bandwidth of 1.75(25) GHz at 6 μm.

For every laser frequency, an accumulated time spectrum of K_α events was recorded using large-area avalanche photo-diodes[27] (LAAPDs). Their typical time and energy resolutions for 1.9 keV X-rays are 35 ns and 25% (full-width at half maximum), respectively. The resulting X-ray time spectra are shown for laser frequencies on and off resonance in Fig. 4. The large 'prompt' peak contains the ~99% of the muons that do not form metastable $\mu p(2S)$ atoms and proceed directly to the 1S ground state (Fig. 1a). This peak helps to normalize the data for each laser wavelength to the number of μp

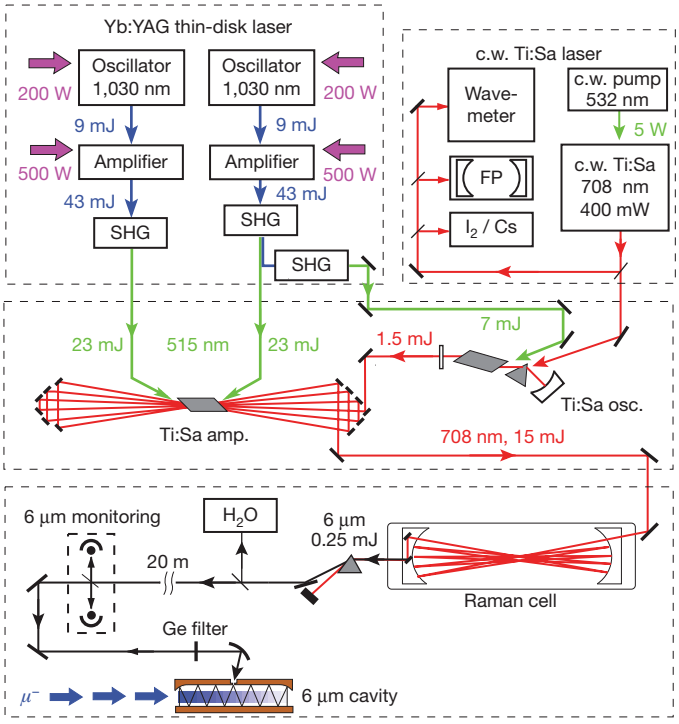

Figure 3 | Laser system. The c.w. light of the Ti:sapphire (Ti:Sa) ring laser (top right) is used to seed the pulsed Ti:sapphire oscillator ('osc.'; middle). A detected muon triggers the Yb:YAG thin-disk lasers (top left). After second harmonic generation (SHG), this light pumps the pulsed Ti:Sa oscillator and amplifier ('amp.'; middle) which emits 5 ns short pulses at the wavelength given by the c.w. Ti:Sa laser. These short pulses are shifted to the required $\lambda \approx 6\,\mu m$ via three sequential Stokes shifts in the Raman cell (bottom). The c.w. Ti:Sa is permanently locked to a I_2/Cs calibrated Fabry-Perot reference cavity (FP). Frequency calibration is always performed at $\lambda = 6\,\mu m$ using H_2O absorption. See Online Methods for details.

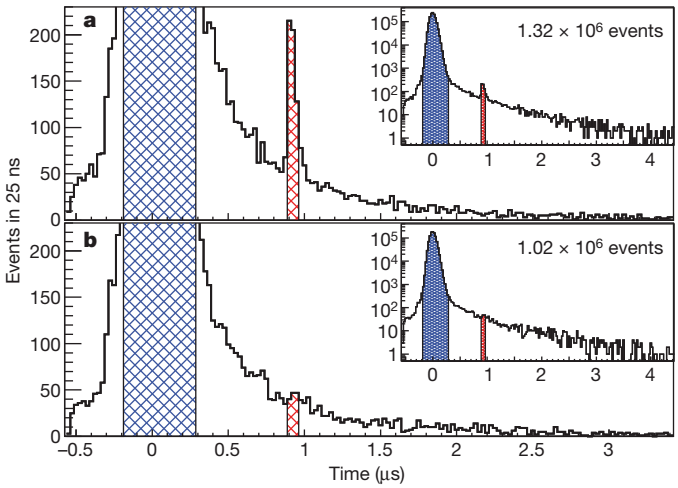

Figure 4 | Summed X-ray time spectra. Spectra were recorded on resonance (**a**) and off resonance (**b**). The laser light illuminates the muonic atoms in the laser time window $t \in [0.887, 0.962]$ μs indicated in red. The 'prompt' X-rays are marked in blue (see text and Fig. 1). Inset, plots showing complete data; total number of events are shown.

atoms formed. The measurement times varied between 3 and 13 h per laser wavelength. The 75-ns-long laser time window, in which the laser induced K_α events are expected, is indicated in Fig. 4. We have recorded a rate of 7 events per hour in the laser time window when on resonance. The background of about 1 event per hour originates mainly from falsely identified muon-decay electrons and effects related to delayed muon transfer to target walls.

Figure 5 shows the measured 2S–2P resonance curve. It is obtained by plotting the number of K_α events recorded in the laser time window, normalized to the number of events in the prompt peak, as a function of the laser frequency. In total, we have measured 550 events in the resonance, where we expect 155 background events. The fit to the data is a Lorentzian resonance line on top of a flat background. All four parameters (Lorentzian amplitude, position and width, as well as background amplitude) were varied freely. A maximum likelihood fit using CERN's ROOT analysis tool accounted for the statistics at each laser wavelength. Our statistical uncertainties are the 1σ confidence intervals.

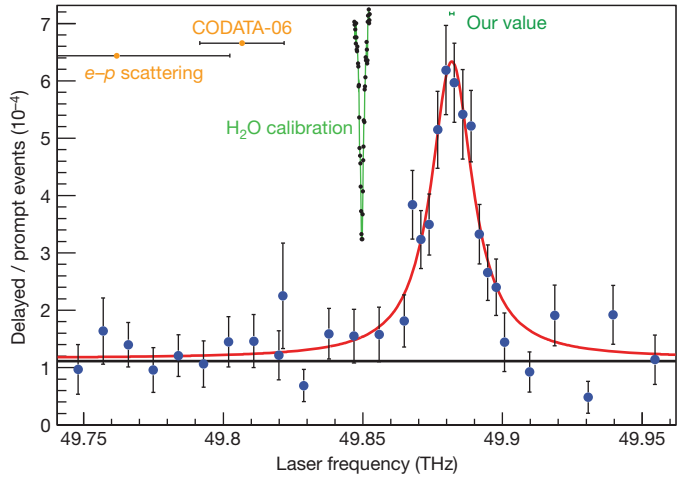

Figure 5 | Resonance. Filled blue circles, number of events in the laser time window normalized to the number of 'prompt' events as a function of the laser frequency. The fit (red) is a Lorentzian on top of a flat background, and gives a χ^2/d.f. of 28.1/28. The predictions for the line position using the proton radius from CODATA[3] or electron scattering[1,2] are indicated (yellow data points, top left). Our result is also shown ('our value'). All error bars are the ±1 s.d. regions. One of the calibration measurements using water absorption is also shown (black filled circles, green line).

We obtain a centroid position of 49,881.88(70) GHz, and a width of 18.0(2.2) GHz, where the given uncertainties are the 1 s.d. statistical uncertainties. The width compares well with the value of 20(1) GHz expected from the laser bandwidth and Doppler- and power-broadening of the natural line width of 18.6 GHz. The resulting background amplitude agrees with the one obtained by a fit to data recorded without laser (not shown). We obtain a value of $\chi^2 = 28.1$ for 28 degrees of freedom (d.f.). A fit of a flat line, assuming no resonance, gives $\chi^2 = 283$ for 31 d.f., making this resonance line 16σ significant.

The systematic uncertainty of our measurement is 300 MHz. It originates exclusively from our laser wavelength calibration procedure. We have calibrated our line position in 21 measurements of 5 different water vapour absorption lines in the range $\lambda = 5.49$–6.01 μm. The positions of these water lines are known[28] to an absolute precision of 1 MHz and are tabulated in the HITRAN database[29]. The measured relative spacing between the 5 lines agrees with the published ones. One such measurement of a water vapour absorption line is shown in Fig. 5. Our quoted uncertainty of 300 MHz comes from pulse to pulse fluctuations and a broadening effect occurring in the Raman process. The FSR of the reference Fabry–Perot cavity does not contribute, as the FSR is known better than 3 kHz and the whole scanned range is within 70 FSR of the water line. Other systematic corrections we have considered are Zeeman shift in the 5 T field (<30 MHz), a.c. and d.c. Stark shifts (<1 MHz), Doppler shift (<1 MHz) and pressure shift (<2 MHz). Molecular effects do not influence our resonance position because the formed muonic molecules $pp\mu^+$ are known to de-excite quickly[30] and do not contribute to our observed signal. Also, the width of our resonance line agrees with the expected width, whereas molecular lines would be wider.

The centroid position of the $2S^{F=1}_{1/2} - 2P^{F=2}_{3/2}$ transition is 49,881.88(76) GHz, where the uncertainty is the quadratic sum of the statistical (0.70 GHz) and the systematic (0.30 GHz) uncertainties. This frequency corresponds to an energy of $\Delta\tilde{E} = 206.2949(32)$ meV. From equation (1), we deduce an r.m.s. proton charge radius of $r_p = 0.84184(36)(56)$ fm, where the first and second uncertainties originate respectively from the experimental uncertainty of 0.76 GHz and the uncertainty in the first term in equation (1). Theory, and here mainly the proton polarizability term, gives the dominant contribution to our total relative uncertainty of 8×10^{-4}. Our experimental precision would suffice to deduce r_p to 4×10^{-4}.

This new value of the proton radius $r_p = 0.84184(67)$ fm is 10 times more precise, but 5.0σ smaller, than the previous world average[3], which is mainly inferred from H spectroscopy. It is 26 times more accurate, but 3.1σ smaller, than the accepted hydrogen-independent value extracted from electron–proton scattering[1,2]. The origin of this large discrepancy is not known.

If we assume some QED contributions in μp (equation (1)) were wrong or missing, an additional term as large as 0.31 meV would be required to match our measurement with the CODATA value of r_p. We note that 0.31 meV is 64 times the claimed uncertainty of equation (1).

The CODATA determination of r_p can be seen in a simplified picture as adjusting the input parameters r_p and R_∞ (the Rydberg constant) to match the QED calculations[8] to the measured transition frequencies[4–7] in H: 1S–2S on the one hand, and $2S - n\ell$ ($n\ell = 2P,4,6,8S/D,12D$) on the other.

The 1S–2S transition in H has been measured[3–5] to 34 Hz, that is, 1.4×10^{-14} relative accuracy. Only an error of about 1,700 times the quoted experimental uncertainty could account for our observed discrepancy. The $2S - n\ell$ transitions have been measured to accuracies between 1/100 (2S–8D) (refs 6, 7) and 1/10,000 ($2S_{1/2}$–$2P_{1/2}$ Lamb shift[31]) of the respective line widths. In principle, such an accuracy could make these data subject to unknown systematic shifts. We note, however, that all of the ($2S - n\ell$) measurements (for a list, see, for example, table XII in ref. 3) suggest a larger proton charge radius. Finally, the origin of the discrepancy with the H data could originate

from wrong or missing QED terms or from unexpectedly large contributions of yet uncalculated higher order terms.

Dispersion analysis of the nucleon form factors has recently[32] also produced smaller values of $r_p \in [0.822...0.852]$ fm, in agreement with our accurate value.

Assuming now the correctness of the Lamb shift calculations for μp (refs 8, 11–15) and H (refs 8, 9) atoms, we use the precisely measured H(1S–2S) interval[4,5], the H(1S)- and H(2S)-Lamb shifts calculated with our r_p value, and the most recent value of the fine structure constant[33], to obtain a new value of the Rydberg constant, $R_\infty = 10{,}973{,}731.568160(16)\,\mathrm{m}^{-1}$ (1.5 parts in 10^{12}). This is $-110\,\mathrm{kHz}/c$ or 4.9σ away from the CODATA value[3], but 4.6 times more precise.

Spectroscopy in hydrogenic atoms continues to challenge our understanding of physics. New insight into the present proton radius discrepancy is expected to come from additional data we have recorded in muonic hydrogen and deuterium, and from our new project, the measurement of the Lamb shift in muonic helium ions.

METHODS SUMMARY

Slow negative muons from our low-energy muon beam line[17] are magnetically guided into a 5 T solenoid, where individual muons are detected (Fig. 2), providing the laser trigger. The muon stops inside a target filled with 1 hPa of H_2 gas and forms a μp atom. Meanwhile, the frequency-doubled light from a fast pulsed Yb:YAG disk laser[22,23] pumps a pulsed Ti:sapphire oscillator-amplifier laser which is c.w.-seeded by a Ti:sapphire ring laser[24,25] (Fig. 3). The Ti:sapphire pulses at $\lambda \approx 708$ nm are converted to the required $\lambda \approx 6\,\mu$m light via three sequential Stokes shifts in a Raman cell[26] filled with 15.5 bar H_2.

The 6 μm pulses are transported to the muon beam area and injected into a multi-pass cavity surrounding the muon stop volume inside the H_2 target. On resonance, the muonic 2S–2P can be excited, which is immediately followed by the muonic 2P–1S K_α transition at 1.9 keV energy. The 1.9 keV K_α X-rays are detected in 20 LAAPDs[27].

The number of 1.9 keV X-rays occurring at the time when the laser pulse circulates inside the target cavity (Fig. 4) is the signature of our transition. The resonance line in Fig. 5 is obtained by normalizing the number of K_α X-rays in the time window by the number of μp atoms formed.

Full Methods and any associated references are available in the online version of the paper at www.nature.com/nature.

1. Sick, I. On the rms-radius of the proton. *Phys. Lett. B* **576,** 62–67 (2003).
2. Blunden, P. G. & Sick, I. Proton radii and two-photon exchange. *Phys. Rev. C* **72,** 057601 (2005).
3. Mohr, P. J., Taylor, B. N. & Newell, D. B. CODATA recommended values of the fundamental physical constants: 2006. *Rev. Mod. Phys.* **80,** 633–730 (2008).
4. Niering, M. *et al.* Measurement of the hydrogen 1*S* - 2*S* transition frequency by phase coherent comparison with a microwave cesium fountain clock. *Phys. Rev. Lett.* **84,** 5496–5499 (2000).
5. Fischer, M. *et al.* New limits on the drift of fundamental constants from laboratory measurements. *Phys. Rev. Lett.* **92,** 230802 (2004).
6. de Beauvoir, B. *et al.* Metrology of the hydrogen and deuterium atoms: determination of the Rydberg constant and Lamb shifts. *Eur. Phys. J. D* **12,** 61–93 (2000).
7. Schwob, C. *et al.* Optical frequency measurement of the 2*S* – 12*D* transitions in hydrogen and deuterium: Rydberg constant and Lamb shift determinations. *Phys. Rev. Lett.* **82,** 4960–4963 (1999).
8. Eides, M. I., Grotch, H. & Shelyuto, V. A. Theory of light hydrogenlike atoms. *Phys. Rep.* **342,** 63–261 (2001).
9. Karshenboim, S. G. Precision physics of simple atoms: QED tests, nuclear structure and fundamental constants. *Phys. Rep.* **422,** 1–63 (2005).
10. Lamb, W. E. & Retherford, R. C. Fine structure of the hydrogen atom by a microwave method. *Phys. Rev.* **72,** 241–243 (1947).
11. Pachucki, K. Theory of the Lamb shift in muonic hydrogen. *Phys. Rev. A* **53,** 2092–2100 (1996).
12. Pachucki, K. Proton structure effects in muonic hydrogen. *Phys. Rev. A* **60,** 3593–3598 (1999).
13. Borie, E. Lamb shift in muonic hydrogen. *Phys. Rev. A* **71,** 032508 (2005).
14. Martynenko, A. P. 2S Hyperfine splitting of muonic hydrogen. *Phys. Rev. A* **71,** 022506 (2005).
15. Martynenko, A. P. Fine and hyperfine structure of P-wave levels in muonic hydrogen. *Phys. At. Nucl.* **71,** 125–135 (2008).
16. Pachucki, K. & Jentschura, U. D. Two-loop Bethe-logarithm correction in hydrogenlike atoms. *Phys. Rev. Lett.* **91,** 113005 (2003).
17. Antognini, A. *et al.* The 2S Lamb shift in muonic hydrogen and the proton rms charge radius. *AIP Conf. Proc.* **796,** 253–259 (2005).
18. Jensen, T. S. & Markushin, V. E. Collisional deexcitation of exotic hydrogen atoms in highly excited states. *Eur. Phys. J. D* **21,** 261–270 (2002).
19. Pohl, R. 2S state and Lamb shift in muonic hydrogen. *Hyp. Interact.* **193,** 115–120 (2009).
20. Pohl, R. *et al.* Observation of long-lived muonic hydrogen in the 2S state. *Phys. Rev. Lett.* **97,** 193402 (2006).
21. Pohl, R. *et al.* The muonic hydrogen Lamb-shift experiment. *Can. J. Phys.* **83,** 339–349 (2005).
22. Antognini, A. *et al.* Thin-disk Yb:YAG oscillator-amplifier laser, ASE, and effective Yb:YAG lifetime. *IEEE J. Quantum Electron.* **45,** 993–1005 (2009).
23. Giesen, A. *et al.* Scalable concept for diode-pumped high-power solid-state lasers. *Appl. Phys. B* **58,** 365–372 (1994).
24. Antognini, A. *et al.* Powerful fast triggerable 6 μm laser for the muonic hydrogen 2S-Lamb shift experiment. *Opt. Commun.* **253,** 362–374 (2005).
25. Nebel, T. *et al.* Status of the muonic hydrogen Lamb-shift experiment. *Can. J. Phys.* **85,** 469–478 (2007).
26. Rabinowitz, P., Perry, B. & Levinos, N. A continuously tunable sequential Stokes Raman laser. *IEEE J. Quantum Electron.* **22,** 797–802 (1986).
27. Ludhova, L. *et al.* Planar LAAPDs: temperature dependence, performance, and application in low-energy x-ray spectroscopy. *Nucl. Instrum. Methods A* **540,** 169–179 (2005).
28. Toth, R. A. Water vapor measurements between 590 and 2582 cm^{-1}: Line positions and strengths. *J. Mol. Spectrosc.* **190,** 379–396 (1998).
29. Rothman, L. S. *et al.* The HITRAN 2008 molecular spectroscopic database. *J. Quant. Spectrosc. Radiat. Transf.* **110,** 533–572 (2009).
30. Kilic, S., Karr, J.-P. & Hilico, L. Coulombic and radiative decay rates of the resonances of the exotic molecular ions *ppμ, ppπ, ddμ, ddπ,* and *dtμ. Phys. Rev. A* **70,** 042506 (2004).
31. Lundeen, S. R. & Pipkin, F. M. Measurement of the Lamb shift in hydrogen, n=2. *Phys. Rev. Lett.* **46,** 232–235 (1981).
32. Belushkin, M. A., Hammer, H.-W. & Meissner, U.-G. Dispersion analysis of the nucleon form factors including meson continua. *Phys. Rev. C* **75,** 035202 (2007).
33. Hanneke, D., Fogwell, S. & Gabrielse, G. New measurement of the electron magnetic moment and the fine structure constant. *Phys. Rev. Lett.* **100,** 120801 (2008).

Acknowledgements We thank L. Simons and B. Leoni for setting up the cyclotron trap, H. Brückner, K. Linner, W. Simon, O. Huot and Z. Hochman for technical support, P. Maier-Komor, K. Nacke, M. Horisberger, A. Weber, L. Meier and J. Hehner for thin foils and windows, N. Schlumpf, U. Hartmann and M. Gaspar for electronics, S. Spielmann-Jaeggi and L. Carroll for optical measurements, Ch. Parthey and M. Herrmann for their help, the MEG-collaboration for a share of beam-time, and A. Voss, B. Weichelt and J. Fruechtenicht for the loan of a laser pump diode. We acknowledge the essential contributions of H. Hofer and V.W. Hughes in the initial stages of the experiment. We also thank the PSI accelerator division, the Hallendienst, the workshops at PSI, MPQ and Fribourg, and other support groups for their help. We acknowledge support from the Max Planck Society and the Max Planck Foundation, the Swiss National Science Foundation (project 200020-100632) and the Swiss Academy of Engineering Sciences, the BQR de l'UFR de physique fondamentale et appliquée de l'Université Paris 6, the program PAI Germaine de Staël no. 07819NH du ministère des affaires étrangères France, and the Fundação para a Ciência e a Tecnologia (Portugal) and FEDER (project PTDC/FIS/82006/2006 and grant SFRH/BPD/46611/2008). P.I. and E.-O.L.B. acknowledge support from the 'ExtreMe Matter Institute, Helmholtz Alliance HA216/EMMI'.

Author Contributions R.P., A.A., F.N., F.D.A., F.B., A.D., A.G., T.G., T.W.H., L.J., C.-Y.K., Y.-W.L., T.N., P.R., K.S., C.S. and F.K. designed, built and operated parts of the laser system. R.P., A.A., F.N., D.S.C., L.M.P.F., P.K., Y.-W.L., J.A.M.L., L.L., C.M.B.M., F.M., T.N., J.M.F.d.S., L.A.S., K.S., D.T., J.F.C.A.V. and F.K. planned, built and set up the various detectors of the experiment. R.P., A.A., D.S.C., F.M., D.T., J.F.C.A.V. and F.K. designed, built, set up and operated the muon beam line. R.P., A.A., F.N., J.M.R.C., D.S.C., A.D., S.D., L.M.P.F., C.-Y.K., P.K., Y.-W.L., F.M., T.N., J.M.F.d.S., K.S., D.T., J.F.C.A.V. and F.K. designed and implemented the electronics used in the experiment. R.P., A.A., J.M.R.C., P.I., P.K., E.-O.L.B. and T.N. set up the computing infrastructure, wrote software and realized the data acquisition system. R.P., A.A., F.N., F.D.A. F.B., J.M.R.C., D.S.C., A.D., L.M.P.F., P.I., L.J., C.-Y.K., P.K., E.-O.L.B., Y.-W.L., J.A.M.L., L.L., C.M.B.M., F.M., T.N., J.M.F.d.S., K.S., C.S., D.T., J.F.C.A.V. and F.K. took part in the months-long data-taking runs. E.-O.L.B., P.I. and F.K. did work on QED theory. R.P., A.A., F.N., F.B., P.I., L.J., P.K., L.L., T.N., D.T. and F.K. analysed the data and wrote the initial manuscript. The manuscript was then read, improved and finally approved by all authors.

METHODS

The low-energy muon beam line[17] at PSI consists of the cyclotron trap (CT), the muon extraction channel (MEC), and the 5 T solenoid containing the elements depicted in Fig. 2. The CT is a magnetic bottle made from two 4 T ring coils, with $B = 2$ T in the centre of the CT. Negative pions (10^8 s^{-1}) enter the CT tangentially and are moderated in a degrader. About 30% of the pions decay into μ^- which are further decelerated by repeatedly passing a metallized thin Formvar foil placed in the centre of the CT. A high voltage of -20 kV is applied to the Formvar foil. The μ^- are confined in the magnetic bottle until this repulsive electric field dominates over the magnetic forces. Muons leave the CT close to the axis and enter the MEC, a toroidal momentum filter (magnetic field $B = 0.15$ T) which favours muons with $\sim$20 keV energy and separates them from background radiation. From the MEC, the muons are guided into the bore hole of a 5 T superconducting magnet, slightly above its axis. The solenoid's high magnetic field ensures minimal radial size of the muon beam, thereby reducing the target volume to be illuminated by the laser. Before entering the hydrogen target, the muons pass two stacks of ultra-thin carbon foils (area density $d = 4\,\mu$g cm^{-2}) kept at high electric potential that both serve as muon detectors and decelerate the muons to 3–6 keV. Each muon releases a few electrons in the stack-foils which are separated from the much slower muons in an $\mathbf{E}\times\mathbf{B}$ separator field. The electrons are detected by plastic scintillators and photomultiplier tubes and provide the trigger signal for the data acquisition system and the laser.

Finally, the muons arrive in the gas target volume which is filled with 1.0 hPa of H_2 gas at a temperature of 20 °C and has a length of 20 cm along the beam axis. The transverse dimensions of the stop volume are 5×12 mm^2. Above and below, two face-to-face rows of 10 LAAPDs[27] (14×14 mm^2 active area) record the 1.9 keV K_α X-rays in a distance of 8 mm from the muon beam axis, providing an effective solid angle coverage of 20% of 4π. To improve the energy resolution and the signal-to-noise ratio, the LAAPDs are cooled to -30 °C. They have been optimized for the detection of the 1.9 keV X-rays from the μp(2P$\rightarrow$1S) transition, but they are also sensitive to the muon decay electrons. In addition, plastic scintillators have been installed to increase the detection efficiency for decay electrons, whose appearance with some delay following a 2 keV X-ray signal is required in the data analysis to reduce the background. The LAAPD signals are read out using VME waveform digitizers.

The muonic hydrogen formed inside the gas target is illuminated by the 6 μm laser pulse. The laser system has to deliver pulses of 0.25 mJ at 6 μm, and has to be stochastically triggerable, with average rates of $\sim$400 s^{-1} and with a delay between trigger and arrival of the pulse inside the cavity of <1 μs. Additionally, the laser has to be tunable from 6.0 to 6.03 μm with a bandwidth <2 GHz to search for and scan the resonance. The muon entrance detectors trigger an Yb:YAG thin-disk laser, made from two parallel systems, each composed of a *Q*-switched oscillator and a 12-pass amplifier. A fibre coupled diode laser continuously pumps the thin-disk laser with 1.4 kW of radiation at 940 nm, so that the energy is continuously stored in the disk active material. When receiving a muon-trigger, the *Q*-switched oscillator cavities are closed causing a fast intra-cavity pulse build-up. The circulating power is released when the cavities are opened, each delivering a 9 mJ pulse at 1,030 nm with a beam propagation factor $M^2 < 1.1$ and a delay of only 250 ns. Such a short delay is achieved by operating the cavities in a c.w.-prelasing mode. The two parallel thin-disk amplifiers boost each pulse to 43 mJ using a non-common configuration whose main peculiarity is its insensitivity to thermal lens effects even for large beam waists[22]. A frequency doubling stage based on LBO crystals is used to convert the two disk laser pulses from 1,030 nm to 515 nm, which is a suitable wavelength for the pumping of the Ti:sapphire pulsed laser.

The pulsed Ti:sapphire laser consists of a wavelength-selective master-oscillator cavity, lasing at 708 nm, and a multi-pass power-amplifier in bow-tie configuration. The pulsed Ti:sapphire system is pumped with a total of 53 mJ at $\lambda = 515$ nm. The frequency of the pulsed Ti:sapphire laser is controlled by injection seeding the Ti:sapphire oscillator with a single-mode c.w. Ti:sapphire laser, the stability of which is guaranteed by locking it to an external reference Fabry–Perot cavity. This cavity was calibrated by means of well known I_2, Rb and Cs lines. The resulting free spectral range was measured to be 1,497.332(3) MHz in the 708 nm region. The frequency of the c.w. Ti:sapphire laser is thus absolutely known with a precision of 10 MHz. Apart from a frequency chirp of 100 MHz occurring in the pulsed Ti:sapphire laser, the frequency of the pulsed Ti:sapphire laser equals the frequency of the c.w. one. The 1.5 mJ pulses emitted from the oscillator cavity have a pulse length of 5.5 ns, which is optimal for efficient Raman conversion.

After amplification, the Ti:sapphire pulses with 15 mJ energy are coupled into a Raman-shifter[26] operated with 15.5 bar H_2. Therein within 60 m (31 passes, with refocusing at each pass) the red light at 708 nm is converted to 6 μm in three sequential Stokes shifts. The output frequency of the Raman cell ν_{out} is given by $\nu_{\mathrm{out}} = \nu_{\mathrm{in}} - 3\Delta_{\mathrm{vib}}$, where ν_{in} is the frequency of the Ti:sapphire laser pulse and $\Delta_{\mathrm{vib}} = c \times 4{,}155.22(2)$ cm^{-1}, the excitation energy of the first vibrational level in hydrogen. Tuning the wavelength of the c.w. Ti:sapphire laser therefore leads to a tuning of the frequency of the pulses exiting the Raman cell. In order to avoid uncertainties related to chirping effects in the Ti:sapphire laser and to the Stokes shift (Δ_{vib}), the frequency calibration of the laser pulses leaving the Raman cell is performed directly at 6 μm by means of water vapour absorption spectroscopy. In this way, the frequency of the pulse we use to drive the 2S–2P resonance is known over the whole scan range with a precision of 300 MHz.

The 6 μm laser pulse is finally coupled into a non-resonant multipass cavity[21] surrounding the muon stop volume. This cavity was designed to be very insensitive to misalignments and to illuminate a large volume. The laser pulse enters the cavity via a 0.6-mm-diameter hole in one of the mirrors. The pulse inside the cavity undergoes 1,000 reflections between the two cavity mirrors, which leads to a relatively homogeneous illumination of the volume enclosed by the cavity mirrors. The measured confinement time of the light is 50 ns and the estimated laser fluence is 6 mJ cm^{-2}. This confinement time results from the losses through the injection hole and the mirror reflectivity ($R = 99.9\%$).